








## A new approach to constraining properties of AGN host galaxies by combining image and SED decomposition: testing upon the $M_{\text{BH}} - M_{\star}$ relation

HAORAN YU (于浩然) <sup>1,2</sup> LULU FAN (范璐璐) <sup>1,2,3</sup> YUNKUN HAN (韩云坤) <sup>4,5,6,7</sup>  
WEIBIN SUN (孙卫斌) <sup>1,2</sup> YIHANG ZHANG (张迺航) <sup>1,2</sup> XUHENG DING (丁旭恒) <sup>8</sup> AND  
YONGQUAN XUE (薛永泉) <sup>1,2</sup>

<sup>1</sup>CAS Key Laboratory for Research in Galaxies and Cosmology, Department of Astronomy, University of Science and Technology of China, Hefei 230026, China

<sup>2</sup>School of Astronomy and Space Science, University of Science and Technology of China, Hefei 230026, China

<sup>3</sup>Deep Space Exploration Laboratory, Hefei 230088, China

<sup>4</sup>Yunnan Observatories, Chinese Academy of Sciences, 396 Yangfangwang, Guandu District, Kunming, 650216, P. R. China

<sup>5</sup>Center for Astronomical Mega-Science, Chinese Academy of Sciences, 20A Datun Road, Chaoyang District, Beijing, 100012, P. R. China

<sup>6</sup>Key Laboratory for the Structure and Evolution of Celestial Objects, Chinese Academy of Sciences, 396 Yangfangwang, Guandu District, Kunming, 650216, P. R. China

<sup>7</sup>International Centre of Supernovae, Yunnan Key Laboratory, Kunming 650216, P. R. China

<sup>8</sup>School of Physics and Technology, Wuhan University, Wuhan 430072, China

Submitted to AAS Journal

### ABSTRACT

The outshining light from active galactic nuclei (AGNs) poses significant challenges in studying the properties of AGN host galaxies. To address this issue, we propose a novel approach which combines image decomposition and spectral energy distribution (SED) decomposition to constrain properties of AGN host galaxies. Image decomposition allows us to disentangle optical flux into AGN and stellar components, thereby providing additional constraints on the SED models to derive more refined stellar mass. To test the viability of this approach, we obtained a sample of 24 X-ray selected type-I AGNs with redshifts ranging from 0.73 to 2.47. We estimated the stellar masses for our sample and found that our results are generally consistent with earlier estimates based on different methods. Through examining the posterior distribution of stellar masses, we find that our method could derive better constrained results compared to previous SED decomposition methods. With the derived stellar masses, we further studied the  $M_{\text{BH}} - M_{\star}$  relation of our sample, finding a higher intrinsic scatter in the correlation for our entire sample compared to the local quiescent correlation, which could be caused by a few “black hole monsters” in our sample. We propose that based on our method,

future works could extend to larger samples of high-redshift AGN host galaxies, thereby enhancing our understanding of their properties.

*Keywords:* Active galactic nuclei (16), Galaxy masses (607), Scaling relations (2031), Spectral energy distribution (2129)

## 1. INTRODUCTION

It is widely believed that supermassive black holes (SMBHs) reside in the central regions of most galaxies (e.g., Magorrian et al. 1998; Gebhardt et al. 2001; Kormendy & Ho 2013). Moreover, tight correlations between BH mass ( $M_{\text{BH}}$ ) and properties of the bulge component of the host galaxy (e.g.,  $M_{\text{BH}} - M_{\text{bulge}}$  relation) have been found in the local universe (Ferrarese & Merritt 2000; Marconi & Hunt 2003; Häring & Rix 2004; Bennert et al. 2010; Beifiori et al. 2012; Schramm & Silverman 2013). When it comes to higher redshifts, separating bulge mass from disk mass becomes difficult, making it harder to study the correlation between BH mass and total stellar mass of the host galaxy (e.g., Ding et al. 2020; Suh et al. 2020; Li et al. 2021a; Li et al. 2024; Zhuang & Ho 2023; Tanaka et al. 2024).

In order to explain the origin of this correlation, various theoretical models have been proposed. For example, AGN feedback is invoked in many cosmological simulations, in which a fraction of the AGN energy heats the surrounding gas and regulates the BH accretion and the star formation of the host galaxy (Springel et al. 2005; Di Matteo et al. 2008; Hopkins et al. 2008; DeGraf et al. 2015; Harrison 2017). Alternatively, introducing an indirect connection in which the BH accretion and star formation share a common gas supply is viable (Cen 2015; Menci et al. 2016; Anglés-Alcázar et al. 2017). On the other hand, in a cosmic averaging scenario the correlations could be established through mergers based solely on Central Limit Theorem, without involving any close physical connection between the BH and the host galaxy (Peng 2007; Hirschmann et al. 2010; Jahnke & Macciò 2011). However, which of these models is the dominant cause of the mass correlation is still in debate.

In order to investigate the potential coevolution, many observational efforts have been put into studying the correlations between BHs and host galaxies for moderate and high redshifts (e.g., Treu et al. 2004, 2007; Jahnke et al. 2009; Schramm & Silverman 2013; Sun et al. 2015; Park et al. 2015; Suh et al. 2020; Ding et al. 2020; Li et al. 2021a; Zhuang & Ho 2023; Tanaka et al. 2024). However, obtaining either the BH mass or the properties of the host galaxies is fraught with difficulties. The BH mass can be obtained with dynamical method for nearby galaxies, but it becomes difficult with higher redshifts for the demand of high spatial resolution. Although recently there has been dynamically measured BH mass for a quasar with  $z \sim 2$  (Abuter et al. 2024), previous high-redshift BH masses are derived through mainly virial method (e.g., Vestergaard & Peterson 2006; Schulze et al. 2018) for type-I AGNs. Without the obscuration of the dusty torus according to the unified AGN model (Netzer 2015), the accretion disk in a type-I AGN glares and outshines the stellar emission of the host galaxy by far in the optical and ultraviolet (UV) bands, bringing difficulty to separating the stellar component from AGN contamination.

However, there have been several methods to estimate the host stellar masses of these unobscured AGNs. For example, Matsuoka et al. (2015) obtained high signal-to-noise ratio (S/N) optical spectra of 191 broad-line quasars with  $z < 1$  and performed spectral decomposition to derive the velocity

dispersion and the mass of the stellar component. UV to far infrared (FIR) broadband SED decomposition (Zou et al. 2019; Suh et al. 2019, 2020; Sun et al. 2024) was employed to derive stellar properties of AGN host galaxies, mainly through adding an AGN template in the SED models. With recent deep imaging surveys, image decomposition techniques have been employed to disentangle host galaxies from core contamination (Peng et al. 2002; Park et al. 2015; Kim et al. 2017; Ding et al. 2020, 2023; Li et al. 2021a,b; Li et al. 2023, 2024; Zhuang & Ho 2023; Zhuang et al. 2024). In the image decomposition process, the AGN contribution is modeled as a point spread function (PSF) and subtracted from the original image, leaving the emission from the host galaxies. Ding et al. (2020) estimated stellar masses of 32 X-ray selected AGNs based on stellar fluxes obtained through image decomposition. Setoguchi et al. (2024) used image decomposed SED of the stellar components derived by Li et al. (2021a) to mitigate the contamination in determining BH mass. Inspired by the aforementioned works, here we propose a novel method combining image and SED decomposition to better constrain the stellar mass of host galaxies, where we use the fluxes of the AGNs and the host galaxies derived from image decomposition to refine the corresponding models in the UV-FIR broadband SED fitting.

This paper is structured as follows. Section 2 introduces the sample used in this work. Section 3 describes the Bayesian methodology that we utilized to incorporate additional information from image decomposition to constrain SED models. Section 4 compares our stellar mass estimation with previous works and examines the  $M_{\text{BH}} - M_{\star}$  relation for our sample. Section 5 discusses the probable sources of error in our work and the future prospects of our approach. Finally, Section 6 presents the concluding remarks. Throughout the paper, we assume a flat  $\Lambda$ CDM cosmology (Komatsu et al. 2011) with  $\Omega_{\Lambda} = 0.7$ ,  $\Omega_{\text{m}} = 0.3$  and  $H_0 = 70 \text{ km s}^{-1} \text{ Mpc}^{-1}$ . The luminosities are given in units of  $\text{erg s}^{-1}$ .

## 2. SAMPLE AND DATA

We initially selected a sample of moderate-luminosity type-I AGNs from Schulze et al. (2018), hereafter S18, in which the near-infrared spectra of the AGN broad line region (BLR) were measured and the black hole masses and spectroscopic redshifts were determined. The sources in our sample are distributed in the CANDELS fields COSMOS, UDS, and GOODS-S, making it easier to search for legacy multi-band data. For the AGNs with black hole mass derived from  $\text{H}\alpha$  or  $\text{H}\beta$  lines (Trakhtenbrot & Netzer 2012), we searched for available *HST* multi-band imaging data and managed to obtain the UV-FIR broadband photometric data for these AGNs from archival catalogs.

We retrieved multi-band *HST* WFC3/ACS images from the 3D-HST survey (Momcheva et al. 2016). Through crossmatching the S18 catalog and Hubble Source Catalog (Whitmore et al. 2016), we further obtained archival imaging data from MAST Portal. We obtained UV-FIR broadband photometric data for our sample from various archival catalogs, namely *GALEX* (Martin et al. 2005) for UV, *SDSS* (Ahumada et al. 2020) and *PAN-STARRS* (Chambers et al. 2016) for optical, *HST* (Whitmore et al. 2016) for optical/near-infrared (NIR), *UKIRT* (Lawrence et al. 2007; Hambly et al. 2008) and *VISTA* (Cross et al. 2012) for NIR, and *WISE* (Cutri et al. 2021), *Spitzer* and *Herschel* for mid-infrared (MIR) and FIR. We set the matching radius at 1 arcsecond for UV and optical bands. For MIR and FIR bands, given the poorer spatial resolution and pointing precision, we extended the matching radius to 5 arcseconds. Furthermore, we visually inspected the corresponding imaging data and removed the photometric data likely to be contaminated by nearby bright sources.

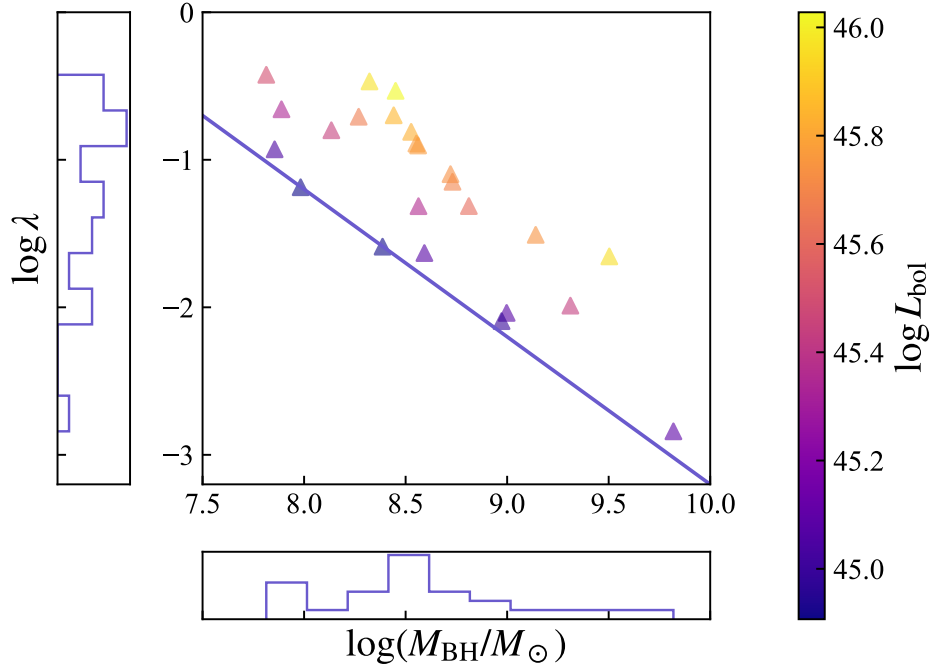


**Figure 1.** Distributions of  $\log(M_{\text{BH}}/M_{\odot})$ ,  $\log \lambda$  and  $\log L_{\text{bol}}$  of the AGNs selected from S18. In the central panel, our samples are plotted in color-mapped triangles. The blue line represents the sources with  $\log L_{\text{bol}} = 44.9$ , which equals to the lower  $L_{\text{bol}}$  limit of our sample. The left and the bottom panels show the marginal distributions of the two parameters, respectively. The color bar on the right maps the bolometric luminosity of the sample.

We employed image decomposition for the matched sources and visually checked the decomposition results. Given the limited imaging quality of the archival data, sources with poorly constrained PSFs tend to yield significantly biased decomposition results and were therefore excluded from further investigation. Our final sample consisted of 24 type-I AGNs, with redshift spanning  $0.72 < z < 2.47$ , black hole mass  $7.81 < \log(M_{\text{BH}}/M_{\odot}) < 9.82$ , Eddington ratio  $-2.84 < \log \lambda < -0.42$  and inferred bolometric luminosity  $44.91 < \log L_{\text{bol}} < 46.02$ . Figure 1 exhibits the properties of the selected BHs, which aids us in correcting for the selection bias.

### 3. METHOD

In this section we illustrate our new method which combines image decomposition and SED decomposition to help to reduce the degeneracy between AGN bright UV-optical emission and host stellar emission. First the image decomposition procedure is briefly introduced in Section 3.1. Then Section 3.2 describes how we use image decomposition results as extra constraints in the UV-FIR broadband SED decomposition.

#### 3.1. *HST* Image decomposition

Following common practice, we simultaneously fitted the two-dimensional flux distribution of the central AGN and the underlying host galaxy, which were modeled as an unresolved point-source component characterized by the PSF and a two-dimensional Sersic profile (e.g., Peng et al. 2002; Park et al. 2015; Kim et al. 2017; Ding et al. 2020; Li et al. 2021a). Although a single Sersic profile may cause uneven residual to be reported when substructures such as spiral arms are present, it acts

as an adequate first-order approximation to estimate the total flux of the stellar component, which has been reported in the literature (Matsuoka et al. 2015; Sun et al. 2015; Suh et al. 2020; Ding et al. 2020; Li et al. 2021a).

We used a state-of-the-art image modeling tool GALIGHT (Ding et al. 2021) to perform the AGN-host galaxy image decomposition. GALIGHT is a Python-based open-source package designed for two-dimensional model fitting of especially large samples of extragalactic sources. It makes use of the image modeling capabilities of LENSTRONOMY (Birrer & Amara 2018), while adding automatic features such as searching for PSF-stars in the field of view, estimating the noise map of the data and identifying objects to set the initial model and associated parameters.

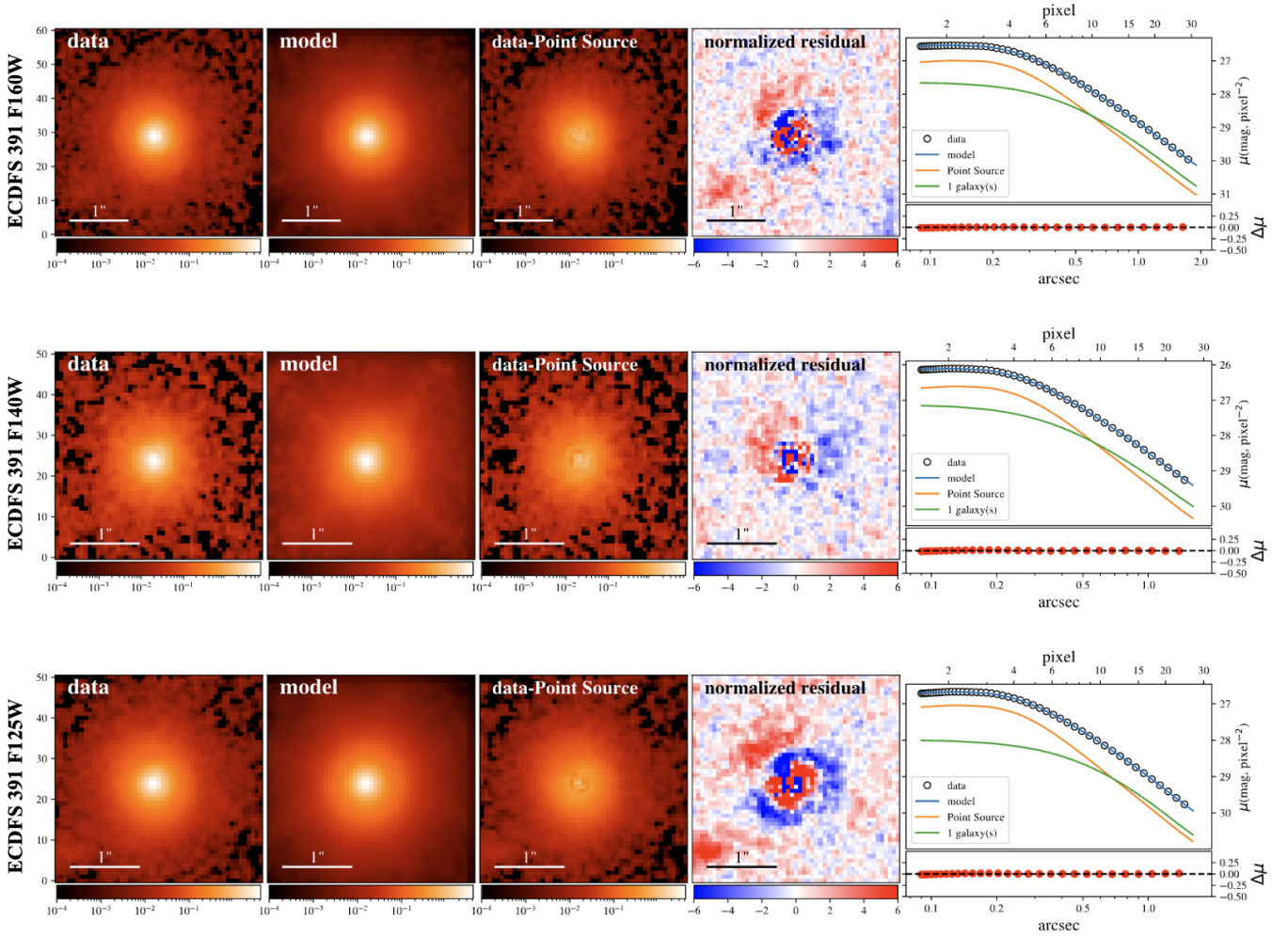


**Figure 2.** Best image decomposition results for ECDFS 391 in F125W, F140W and F160W of *HST* WFC3. The panels from left to right are: (1) observed data, (2) best-fit Sersic + point source model, (3) observed data minus the point source model (i.e., host galaxy and the simultaneously modeled nearby galaxies), (4) residual divided by variance and (5) radial surface brightness profile (top) and residual (bottom). This profile includes the data (open circles), best-fit model (blue curve), the point source model of AGN (orange curve) and the model of 2 galaxies (green curve). The fitting is based on 2-dimensional image, while the 1-dimensional profile is only an illustration of the fitting result.

It has been emphasized that PSF is the dominant source of error in the procedure of flux decomposition (Ding et al. 2020; Tanaka et al. 2024). To minimize the potential effect of PSF-mismatching, we adopted a weighted method from Ding et al. (2020). With the aid of GALIGHT’s automatic PSF searching function, we found isolated and unsaturated point sources within the field of view of each target. We selected the point sources with the top 5 sharpest profiles (i.e. lowest full width at half maximum) as PSFs to be used in the image decomposing routine. We also included the stacked PSFs in the fitting. Using multiple PSFs, we can estimate the uncertainty of the derived fluxes. For a source in a certain band, the weight of each PSF is calculated as

$$w_i = \exp\left(-\alpha \frac{\chi_i^2 - \chi_{\text{best}}^2}{2\chi_{\text{best}}^2}\right), \quad (1)$$

where  $i$  is the rank ordered by  $\chi^2$  from smallest to largest,  $\chi_{\text{best}} = \chi_1$  represents the PSF with the best performance, and  $\alpha$  is an inflation parameter which satisfies the following equation:

$$\alpha \frac{\chi_{\text{worst}}^2 - \chi_{\text{best}}^2}{2\chi_{\text{best}}^2} = 2. \quad (2)$$

The purpose of introducing  $\alpha$  is to avoid too little difference between the relative likelihood of different PSFs. Based on these weights we can calculate the weighted arithmetic mean and the corresponding root mean squared deviation (RMSD) as

$$\bar{x} = \frac{\sum_{i=1}^N x_i \cdot w_i}{\sum_{i=1}^N w_i}, \quad (3)$$

$$\sigma = \sqrt{\frac{\sum_{i=1}^N (x_i - \bar{x})^2 \cdot w_i}{\sum_{i=1}^N w_i}}, \quad (4)$$

where  $N$  is the quantity of PSFs used for the image of this band. For those with less than 4 available PSFs, we fix the RMSD as 10% of the mean value as an estimation. Figure 2 shows the decomposition results for ECDFS 391 in 3 bands. The decomposed fluxes of host galaxy and AGN component are shown in Tables 2 and 3 in the appendix.

### 3.2. SED fitting

By assuming a Gaussian form of noise for all bands, the likelihood function for Bayesian multi-component SED decomposition of galaxy is normally defined as:

$$\begin{aligned} \mathcal{L}(\boldsymbol{\theta}) &\equiv p(\mathbf{d}|\boldsymbol{\theta}, \mathbf{M}, \mathbf{I}) \\ &= p(\mathbf{F}_o^{\text{TOT}}, \mathbf{F}_o^{\text{GAL}}, \mathbf{F}_o^{\text{AGN}}|\boldsymbol{\theta}_1, \boldsymbol{\theta}_2, M_{\text{GAL}}, M_{\text{AGN}}, \mathbf{I}) \\ &= \prod_{i=1}^n \frac{1}{\sqrt{2\pi}\sigma_i} \exp\left(-\frac{1}{2} \frac{(F_{o,i}^{\text{TOT}} - s_1 * f_{m,i}^{\text{GAL}(\boldsymbol{\theta}_1)} - s_2 * f_{m,i}^{\text{AGN}(\boldsymbol{\theta}_2)})^2}{\sigma_i^2}\right), \end{aligned} \quad (5)$$

where  $F_{o,i}^{\text{TOT}}$  and  $\sigma_i$  represent the total observational flux and associated uncertainty in each band,  $f_{m,i}^{\text{GAL}(\boldsymbol{\theta}_1)}$  ( $f_{m,i}^{\text{AGN}(\boldsymbol{\theta}_2)}$ ) represents the flux of the  $i$ -th band predicted by the galaxy (AGN) SED model,  $\boldsymbol{\theta}_1$  and  $s_1$  ( $\boldsymbol{\theta}_2$  and  $s_2$ ) represent the set of free parameters and scaling factor for the galaxy (AGN)

component,  $M_{\text{GAL}}$  ( $M_{\text{AGN}}$ ) represents assumptions involved in the SED modeling of galaxy (AGN), while  $\mathbf{I}$  represents all other relevant background assumptions.

To take advantage of the additional information from image decomposition of host and AGN in  $m$  of  $n$  bands, we define the likelihood function as:

$$\begin{aligned}
\mathcal{L}(\boldsymbol{\theta}) &\equiv p(\mathbf{d}|\boldsymbol{\theta}, \mathbf{M}, \mathbf{I}) \\
&= p(\mathbf{F}_{\text{o}}^{\text{TOT}}, \mathbf{F}_{\text{o}}^{\text{GAL}}, \mathbf{F}_{\text{o}}^{\text{AGN}}|\boldsymbol{\theta}_1, \boldsymbol{\theta}_2, M_{\text{GAL}}, M_{\text{AGN}}, \mathbf{I}) \\
&= \prod_{i=1}^n \frac{1}{\sqrt{2\pi}\sigma_i} \exp\left(-\frac{1}{2} \frac{(F_{\text{o},i}^{\text{TOT}} - s_1 * f_{\text{m},i}^{\text{GAL}}(\boldsymbol{\theta}_1) - s_2 * f_{\text{m},i}^{\text{AGN}}(\boldsymbol{\theta}_2))^2}{\sigma_i^2}\right) \\
&\quad * \prod_{j=1}^m \frac{1}{\sqrt{2\pi}\sigma_j} \exp\left(-\frac{1}{2} \frac{(F_{\text{o},j}^{\text{GAL}} - s_1 * f_{\text{m},j}^{\text{GAL}}(\boldsymbol{\theta}_1))^2}{\sigma_j^2}\right) \\
&\quad * \prod_{k=1}^m \frac{1}{\sqrt{2\pi}\sigma_k} \exp\left(-\frac{1}{2} \frac{(F_{\text{o},k}^{\text{AGN}} - s_2 * f_{\text{m},k}^{\text{AGN}}(\boldsymbol{\theta}_2))^2}{\sigma_k^2}\right),
\end{aligned} \tag{6}$$

$$\tag{7}$$

where  $F_{\text{o},j}^{\text{GAL}}$  and  $\sigma_j$  ( $F_{\text{o},k}^{\text{AGN}}$  and  $\sigma_k$ ) represent the observational flux and associated uncertainty of galaxy (AGN) component in each of the  $m$  bands derived from AGN-host image decomposition. This has been implemented in the new version of BayeSED code (Han & Han 2014, 2018; Han et al. 2023). Compared to the normally defined likelihood in Equation 5, our likelihood additionally constrains the galaxy (AGN) model with the flux obtained through image decomposition.

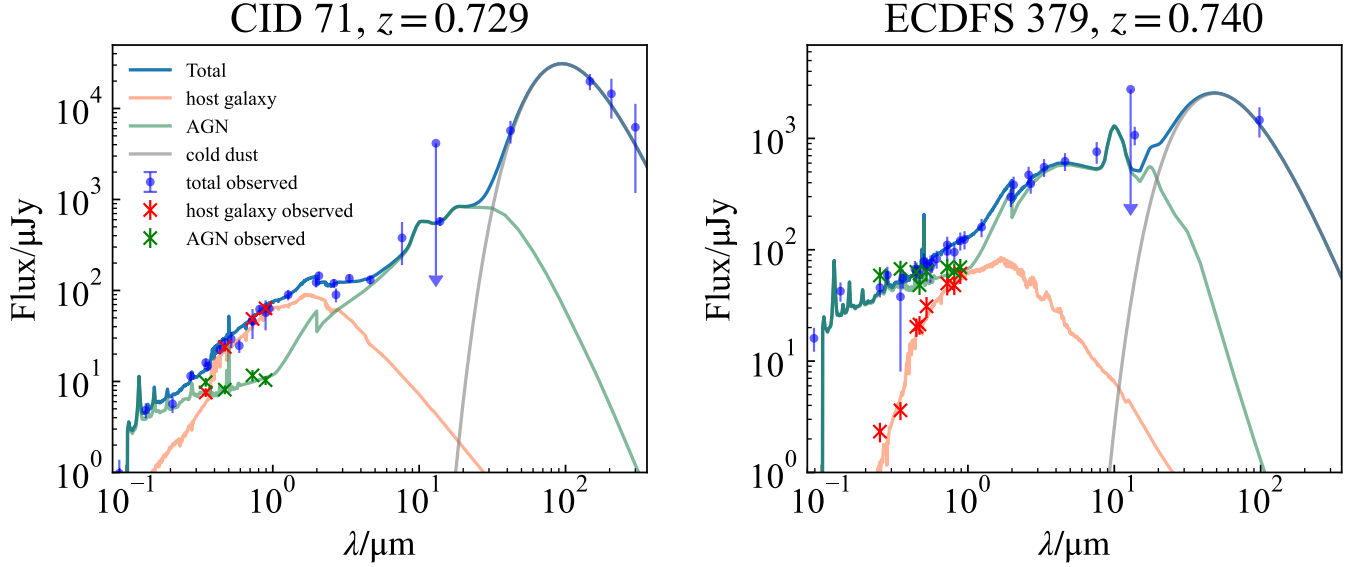
For the SED modeling of the stellar population, we employed the Bruzual & Charlot (2003) simple stellar population (SSP) model with a Chabrier (2003) stellar initial mass function (IMF), the double power law form of star formation history (SFH), and the Calzetti et al. (2000) dust attenuation law. As in Han et al. (2023), we additionally employ a linear SFH-to-metallicity mapping model to describe the chemical evolution history of the galaxy, which has been found to increase the Bayesian evidence of the SED model. Besides, a cold dust component, which is modelled as a gray body, was added with the energy balance assumption in which the total energy of stellar emission absorbed by cold dust is equal to that reemitted in the IR. Finally, the SED of AGN is modelled as the combination of a clumpy torus model and an empirical SED of type-I quasar where an SMC-like dust attenuation law has been applied.

Figure 3 shows two typical SED fitting results, illustrating the circumstances where the stellar or AGN component dominates respectively.

## 4. RESULTS

### 4.1. Stellar mass estimation

Here we compare our stellar mass estimates with those from previous studies which employed different techniques on the same sample. Our sample consists of 24 AGNs, including 6 that also appear in the sample studied by Zou et al. (2019), 4 in the sample studied by Suh et al. (2020), and 6 in the sample studied by Ding et al. (2020) (hereafter Z19, S20 and D20). These overlapping sources are illustrated in Figure 4, with the  $y$ -axis representing our estimates of stellar mass and the  $x$ -axis denoting those from the corresponding comparison samples. The derived stellar masses of our sample are presented in Table 1.



**Figure 3.** Three-component SED decomposition results of CID 71 and ECDFS 379. The spectra have been shifted to rest frame according to the spectroscopic redshifts of the sources. The legend is shown only in the left panel. The orange curves are the stellar population models, assuming star forming history to be double power law. The green curves are the AGN models, which are composed of a clumpy torus model and an empirical type-I quasar template. The gray curves are the models of the cold dust component. The blue dots with error bars are the observed UV-FIR fluxes, while the red and green diagonal crosses are the fluxes of stellar component and AGN inferred from image decomposition. Points downward arrows denote  $1\sigma$  upper limits.

Z19 and S20 used similar methods to address the degeneracy between AGN and stellar components in the UV-optical bands. By assuming energy conservation for galaxies, they constrained stellar emission with FIR photometry. When compared with Z19, who employed the CIGALE (Noll et al. 2009; Boquien et al. 2018) code in the SED fitting, the median absolute difference between our results and theirs is 0.25 dex. We derived consistent stellar masses for 4 sources with  $\log(M_*/M_\odot) > 10.6$ . While for the other 2 sources which have  $\log M_* \sim 10.5$  reported by Z19, we derived values lower than 10. For 3 out of 4 overlapping sources, our results are inconsistent with S20, who utilized a custom SED fitting code. We note that our estimates of stellar mass tend to be lower compared to previous SED decomposition results, which could be caused by the additional constraints of image decomposition fluxes that we introduced in our method.

Our estimation is basically consistent with D20, who fitted the decomposed SED with stellar templates to obtain the stellar masses, with median difference of 0.39 dex. However when comparing the points with identical  $y$ -value in Figure 4, we find that estimates of D20 are basically lower than those given by Z19 and S20. This implies that optical image decomposition and multi-band fluxes may provide inconsistent constraints. Our method combines the advantages of these two methods, thereby the parameter space could be better constrained, which will be discussed in Section 5.2.

#### 4.2. $M_{\text{BH}} - M_*$ relation



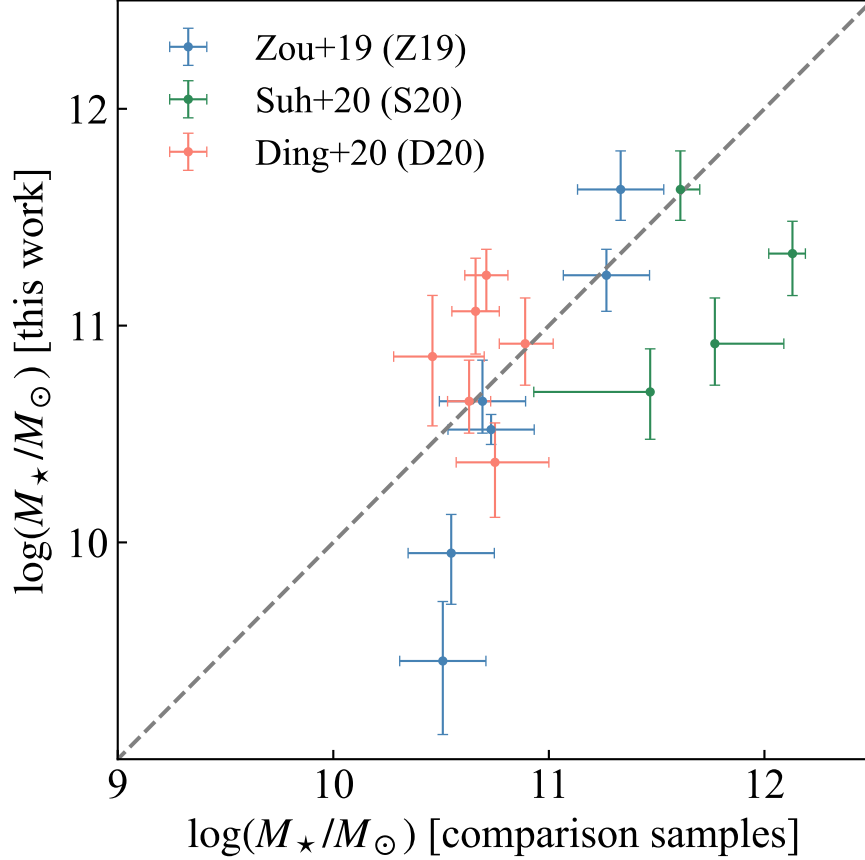


**Figure 4.** The estimates of our host galaxy stellar masses in comparison with Z19, S20 and D20. The  $y$ -values of the points refer to the stellar masses that we derived, while the  $x$ -values indicate the stellar masses given by Z19 (S20, D20) for the blue (green, orange) points. The error bars in both the  $x$  and  $y$ -axis directions denote the corresponding  $1\sigma$  uncertainties. The grey dashed line represents 1:1 relation.

Based on the derived stellar masses, we further investigated the  $M_{\text{BH}} - M_{\star}$  relation for our sample. Due to the fact that the AGN luminosity is likely to depend on black hole mass on a large extent, selection effects are different for our high-redshift sample and the local anchor (Lauer et al. 2007; Schulze & Wisotzki 2011), which means that in the high-redshift sample the AGNs with higher black hole masses are more likely to be selected, biasing the  $M_{\text{BH}} - M_{\star}$  relation. For this reason, we firstly employed Monte Carlo Markov Chain (MCMC) simulation to quantify the bias caused by sample selection as Li et al. (2021a) did. Practically, we created a mock catalog of AGNs based on black hole mass function (BHMF) and Eddington Ratio distribution function (ERDF) which were given in Schulze et al. (2015), then performed a luminosity cut to mimic our bolometric luminosity limited sample, as clarified in Figure 1.

We used an evolutionary model which is

$$\Delta \log M_{\text{BH}} = \gamma \log(1 + z), \quad (8)$$

where  $\Delta \log M_{\text{BH}}$  refers to the difference between the observed black hole mass and the one inferred from the stellar mass with the local relation (Kormendy & Ho 2013), hereafter KH13 relation, while

**Table 1.** Source Catalog

Name	RA	DEC	$z$	$\log M_{\text{BH}}$	$\log M_{\star}$
	(deg)	(deg)		$M_{\odot}$	$M_{\odot}$
(1)	(2)	(3)	(4)	(5)	(6)
CID 108	150.058700	2.477378	1.257450	$8.81 \pm 0.06$	$9.92^{+0.30}_{-0.22}$
CID 110	150.062150	2.455014	0.728313	$8.39 \pm 0.09$	$9.45^{+0.28}_{-0.34}$
CID 128	150.230820	2.578165	1.326690	$9.50 \pm 0.04$	$10.38^{+0.34}_{-0.28}$
CID 192	149.663600	2.085205	1.329610	$8.13 \pm 0.04$	$10.02^{+0.36}_{-0.97}$
CID 1930	150.042450	2.629209	1.408850	$9.14 \pm 0.05$	$11.33^{+0.15}_{-0.19}$
CID 216	149.791790	1.872890	1.369750	$7.85 \pm 0.10$	$10.65^{+0.19}_{-0.15}$
CID 3570	149.641100	2.107600	1.175990	$7.89 \pm 0.06$	$11.23^{+0.12}_{-0.16}$
CID 40	150.199770	2.190852	1.534250	$8.73 \pm 0.24$	$9.17^{+0.10}_{-0.06}$
CID 597	150.526170	2.244970	1.565880	$7.81 \pm 0.10$	$10.86^{+0.28}_{-0.32}$
CID 607	150.609710	2.323110	1.272450	$8.53 \pm 0.03$	$10.37^{+0.18}_{-0.25}$
CID 644	150.511570	2.409609	1.540710	$8.59 \pm 0.05$	$10.69^{+0.20}_{-0.21}$
CID 71	150.123690	2.358250	0.728576	$7.98 \pm 0.03$	$10.52^{+0.07}_{-0.07}$
CID 72	150.091550	2.399045	2.472040	$8.32 \pm 0.67$	$10.66^{+0.22}_{-0.17}$
CID 79	150.173980	2.402966	0.980806	$9.00 \pm 0.05$	$9.95^{+0.18}_{-0.24}$
CID 87	150.133060	2.303255	1.602540	$8.56 \pm 0.37$	$11.63^{+0.18}_{-0.14}$
ECDFS 379	53.112522	-27.684723	0.740331	$9.31 \pm 0.03$	$10.82^{+0.15}_{-0.13}$
ECDFS 391	53.124916	-27.758305	1.221270	$8.72 \pm 0.26$	$10.74^{+0.13}_{-0.09}$
LID 1273	150.056470	1.627495	1.564150	$8.56 \pm 0.02$	$10.92^{+0.21}_{-0.19}$
LID 1820	149.703580	2.578080	1.445400	$8.55 \pm 0.06$	$9.59^{+0.18}_{-0.18}$
LID 360	150.125110	2.861700	1.649980	$8.45 \pm 0.08$	$11.07^{+0.24}_{-0.20}$
SXDS 0328	34.271282	-5.274789	0.807619	$8.97 \pm 0.09$	$10.67^{+0.23}_{-0.20}$
SXDS 0491	34.383537	-5.225608	1.342810	$8.27 \pm 0.03$	$10.97^{+0.26}_{-0.20}$
SXDS 0610	34.469402	-5.259953	0.933160	$9.82 \pm 0.31$	$10.75^{+0.25}_{-0.31}$
SXDS 0735	34.558102	-4.878100	1.345280	$8.44 \pm 0.24$	$10.33^{+0.54}_{-0.58}$

NOTE—Column (1): object name. Columns (2) and (3): right ascension and declination of the object. Columns (4) and (5): spectroscopic redshift and black hole virial mass given by [Schulze et al. \(2018\)](#). Column (6): median stellar mass derived from Bayesian inference, with lower and upper limits indicating 16th and 84th percentiles. A machine readable version of this table is accessible through this [Google drive link](#).

$\gamma$  is the evolution factor. We define  $\sigma_{\mu}$  to be the intrinsic scatter in BH mass. In the sampling process, we generated 100,000 mock AGNs for each set of  $(\gamma, \sigma_{\mu})$  values. We assigned those AGNs with uniformly distributed redshift in the range of  $[0.5, 2.5]$ , then randomly sampled the black hole mass of each AGN ( $M_{\text{BH}}^{\text{mock}}$ ) according to the BHMF. Based on the given redshift and black hole mass of each mock AGN, we then sampled the Eddington ratio to obtain their bolometric luminosity. We removed the mock AGNs which have lower bolometric luminosity than  $\log L_{\text{bol}} = 44.9$  which was the lower limit of our sample, in order to make the mock sample resemble the observed sample as much as possible. Then we assigned the stellar mass ( $M_{\star}^{\text{mock}}$ ) of each mock sample based on the black hole

masses and the intrinsic scatter in BH mass  $\sigma_\mu$  which was added as a random normal variable in the model.

We used likelihood to describe the similarity between the mock sample and the observed sample,

$$\begin{aligned} \mathcal{L} &= \prod_{i=1}^n \mathcal{L}_i \\ &= \prod_{i=1}^n \left( \frac{N[ (|M_\star^{\text{mock}} - M_{\star,i}^{\text{obs}}| < \epsilon_\star) \text{ and } (|M_{\text{BH}}^{\text{mock}} - M_{\text{BH},i}^{\text{obs}}| < \epsilon_{\text{BH}})]}{N[|M_{\text{BH}}^{\text{mock}} - M_{\text{BH},i}^{\text{obs}}| < \epsilon_{\text{BH}}]} \right), \end{aligned} \quad (9)$$

among which  $N[\cdot]$  stands for the quantity of mock sample that satisfies the condition in the bracket.  $n$  refers to the sample size.  $\epsilon_\star$  and  $\epsilon_{\text{BH}}$  were determined from the average  $1\sigma$  estimate error of the observed AGNs, which are 0.29 dex and 0.11 dex, respectively. An analytic derivation of this likelihood function was given by [Schulze & Wisotzki \(2011\)](#).

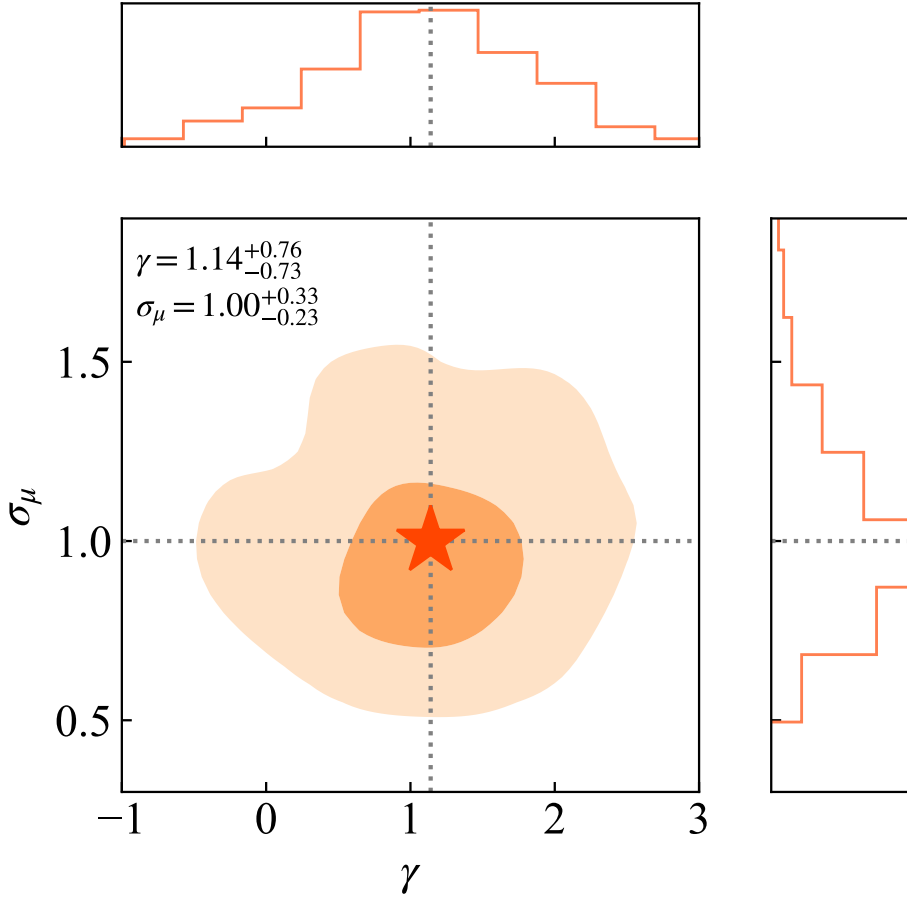


**Figure 5.** The posterior distributions of the evolution factor  $\gamma$  and the intrinsic scatter  $\sigma_\mu$  of the  $M_{\text{BH}} - M_\star$  relation, derived from MCMC simulation assuming flat prior on both parameters. The best inference value is denoted as a red star in the central panel. The shaded areas indicate the 68%, 95% confidence regions of the posterior probability. The top and right panels show the marginal distributions of the MCMC sample.

Based on the likelihood defined above, we derived the posterior distribution, as shown in Figure 5, through MCMC inference assuming flat prior. Note that some similar studies acquired divergent

results under flat prior, thereby they obtained their final result through assuming a log-normal prior on  $\sigma_\mu$  in order to constrain the parameter space (Ding et al. 2020; Li et al. 2021a). Compared with those studies, we derive much higher intrinsic scatter of  $\sigma_\mu = 1.00^{+0.33}_{-0.23}$  (former  $\sigma_\mu \sim 0.3$ ), which may indicate that the black hole and the host galaxy do not grow in lockstep out to  $z \sim 2$  (Yang et al. 2018).

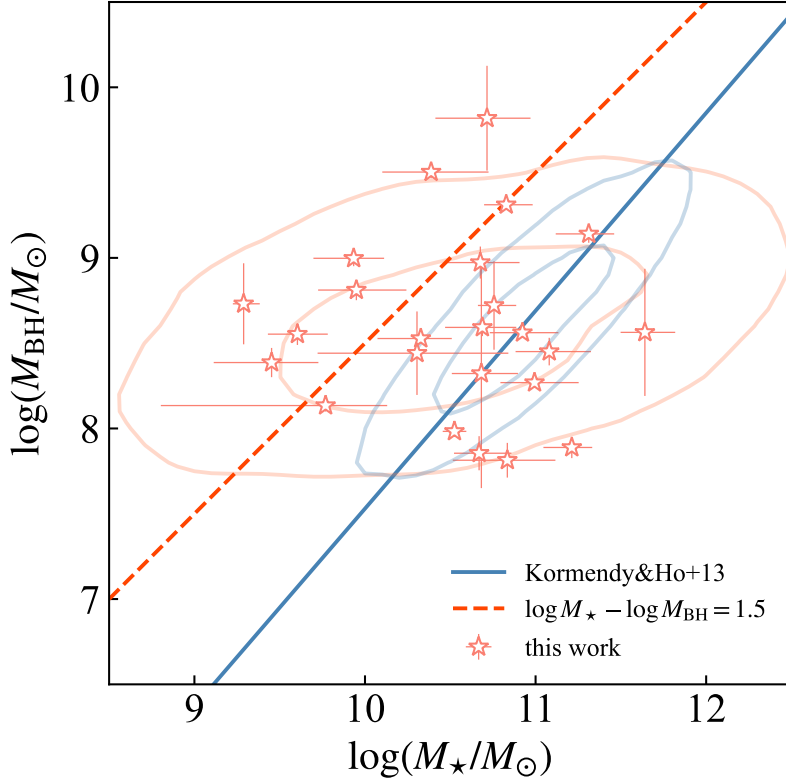


**Figure 6.** The  $M_{\text{BH}} - M_\star$  relation of our sample and the comparison sample. The blue line represents KH13 relation. The red dashed line represents  $\log M_\star - \log M_{\text{BH}} = 1.5$  ( $M_\star$  and  $M_{\text{BH}}$  in units of  $M_\odot$ ). The open orange stars denote our observed sample. The error bars represent the  $1\sigma$  error. The orange contours show 65% and 95% confidence region of the mock sample that we reconstructed with  $\gamma = 1.14$  and  $\sigma_\mu = 1.00$ , while the blue ones represent those reconstructed with KH13 relation parameters of  $\gamma = 0$  and  $\sigma_\mu = 0.29$ .

The  $M_{\text{BH}} - M_\star$  relation is plotted in Figure 6. We adopted medians from the Bayesian SED stellar mass estimation, and the error bars represent the interval between the 16th and 84th percentiles of the Bayesian inference sample. We reconstructed a mock local sample with  $\gamma = 0$  and  $\sigma_\mu = 0.29$  and then applied the same luminosity cut as our observed sample to represent the distribution of the mock sample assuming that the correlation does not evolve at all. Using the model with  $\gamma = 1.14$  and  $\sigma_\mu = 1.00$ , which is the aforementioned best inference parameter set, the distribution of the simulated data points shown as orange contours is consistent with the observed ones. The orange contours span wider range compared with the blue ones, which is mainly due to the larger intrinsic scatter. We note that there are 7 “BH monsters” lying above the red dashed line, with  $\log(M_{\text{BH}}/M_\odot) > \log(M_\star/M_\odot) - 1.5$ . If we ignore these “BH monsters”, the other 17 sources lie evenly around KH13 relation with median difference in  $\log(M_{\text{BH}}/M_\odot)$  of 0.43 dex.

## 5. DISCUSSION

### 5.1. Possible sources of error in our work

Firstly, the multiband fluxes which we use in the SED fitting routine are retrieved from various archival catalogs, which may suffer from inconsistency in photometry. For example, we adopt optical fluxes from Hubble Source Catalog (Whitmore et al. 2016) measured with fixed aperture photometry. In the similar optical bands, however, SDSS catalogs only provide fluxes based on `modelMag` photometry for extended sources, which were derived based on model fitting of De vaucouleur profile or exponential profile. Such inconsistencies may account for the observed fluctuations in the data points across the optical bands of the SED (Figure 3). Data from ground-based infrared telescopes such as *VISTA* and *UKIRT* suffer from low resolution and insufficient pointing precision, which is likely to cause the fluxes to include the contamination from nearby objects.

In the AGN-host galaxy image decomposition procedure, the crucial part is PSF selection (Ding et al. 2020; Tanaka et al. 2024). Mistaking extended sources for PSFs could significantly bias the flux decomposition results, particularly given the limited quality of the imaging data used in our work. Despite this challenge, we employ a weighted method similar to that proposed by Ding et al. (2020), which utilizes multiple PSFs to mitigate the impact of potential mismatched PSFs. Note that Ding et al. (2020) collected all available star-like sources around their 32 sources to construct a PSF library. For each source, they conducted image decomposition using every PSF in the library, ranking the resulting  $\chi^2$  and selecting the top N results in order to cover all possible PSF cases. However, in five out of ten bands which we used for image decomposition the number of available images is less than 5, posing challenges in building comprehensive PSF libraries for these bands. In order to maintain consistency throughout our investigation, we employ an in-between approach for image decomposition, selecting PSFs only from the neighboring regions for each target. While this approach may not capture the full variability in PSFs, it enables us to represent the relative goodness of image decomposition for different sources, which is preferable to coarsely fixing all uncertainties at 10%. Nevertheless, despite setting a lower limit on the estimation error, mismatched PSFs, if present, could still bias the fluxes of the stellar component towards lower values.

### 5.2. Constraining stellar masses

The primary advancement in our method compared to previous multi-band SED decomposition approaches (Zou et al. 2019; Suh et al. 2019, 2020) is the use of image decomposition results as additional constraints to refine SED models. We examined the posterior distribution of stellar masses with and without these extra constraints, denoted as orange and blue curves in Figure 7. Compared to the scenario without constraints, the posterior probability distribution functions (pdfs) with constraints span narrower wings, indicating that the stellar mass is better constrained.

Although image decomposition could pose strong constraints upon host properties, obtaining high-resolution imaging data for high redshift samples often requires significant observing time with space telescopes, limiting the sample size in studies on high-redshift AGN host galaxies. On the other hand, broadband photometric data can be relatively more accessible. Therefore, we further assessed the relative constraints of broadband photometry in different bands. Given the considerable uncertainty in FIR observations, we experimented with a two-component model when fitting the data, excluding *Herschel* Pacs and SPIRE FIR data from the input. The corresponding pdfs are shown as green curves in Figure 7. For CID 71, excluding FIR photometry significantly enlarges the estimation

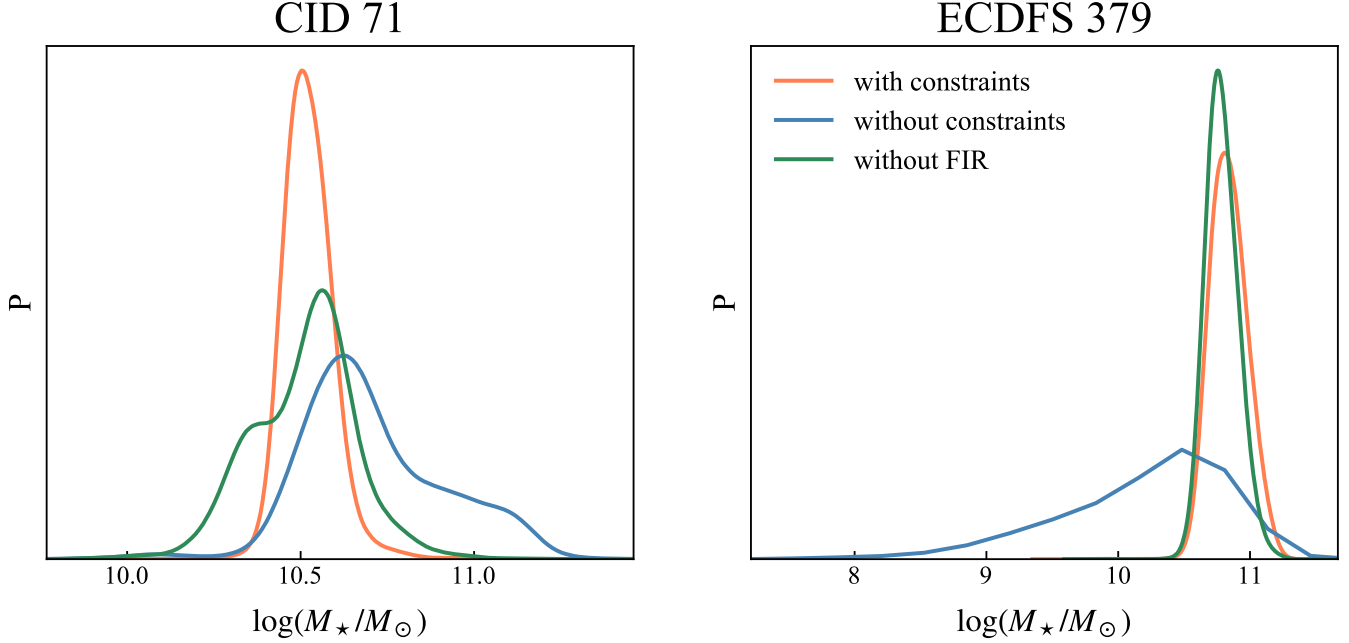


**Figure 7.** Posterior pdf of  $\log(M_*/M_\odot)$ . The legend is shown only in the right panel. The orange curves represent the derived pdf when employing UV-FIR SED decomposition with additional constraints from image decomposition. The blue curves denote the results obtained without these extra constraints (i.e. SED decomposition based solely on broadband photometry). The green curves represent the derived pdf using constraints from image decomposition, but excluding FIR data. The left and right panels show the results for CID 71 and ECDFS 379, respectively, corresponding to the SED decomposition results shown in Figure 3.

error. However, for ECDFS 379, there is only one photometric point in the FIR bands, so excluding FIR makes no difference in the results. As detailed in Section 3.2, the cold dust model is based on the energy balance assumption, thus FIR data provides supplement information about the stellar population. We emphasize that the MIR data offers crucial details about the torus (Netzer 2015) and can put strong constraints on the AGN component, which may help in mitigating the degeneracy between AGN and the stellar component in optical bands. The optical and NIR fluxes can meanwhile provide supplemental information when the image-decomposed bands are insufficient.

Considering that throughout our study we find no clear bias between our sample with 1 or 2 bands of imaging and those with 3 or more bands, we infer that 2 or 3 bands of imaging is sufficient. We propose that future works could base on image decomposition for high-quality imaging data in as few as 3 optical-NIR bands and broadband photometry in other bands, thus expanding the sample size to increase statistical significance. With *JWST* surveys in NIR-MIR ( $4.9 - 28.1\mu\text{m}$ ), investigations on  $z \sim 1.5$  type-I AGNs with much larger samples would become possible.

## 6. SUMMARY

In this work, we proposed a novel method combining image decomposition and SED decomposition to constrain stellar masses. This method enables us to take advantage of limited high-resolution imaging data and mitigate the degeneracy between AGN bright UV-optical emission and host stellar emission as much as possible, constraining host properties in multiple ways. To further test the

viability of this method, we obtained a sample of 24 X-ray selected type-I AGNs, with redshift ranging from 0.73 to 2.47.

The main findings of this work are listed below:

- We compared our stellar mass estimates with previous works which have samples overlapping with ours. We find that our results partially agree with those based on broadband SED decomposition (Zou et al. 2019; Suh et al. 2020), and are generally consistent with those based on image decomposition (Ding et al. 2020).
- We studied the  $M_{\text{BH}} - M_{\star}$  relation of our sample, finding much higher intrinsic scatter for our sample compared to the local  $M_{\text{BH}} - M_{\text{bulge}}$  relation, which may be caused by 7 “BH monsters” in our sample. If these “BH monsters” are excluded, our results basically agree with the local correlation given in Kormendy & Ho (2013).
- We evaluated the impact of various data on the derived posterior pdf of stellar masses. The results show that stellar mass is better constrained when using our method which combines image decomposition data and MIR/FIR broadband photometric data.

We propose that, based on our method which combines image and SED decomposition, future work could rely on as few as 2 or 3 optical-NIR bands for image decomposition and utilize fluxes measured from broadband photometry in any available optical-FIR bands. Our approach would alleviate the demand for high image resolution and facilitate investigations of larger samples, thereby enhancing our understanding of high redshift AGN host galaxies.

1 This work is supported by National Key Research and Development Program of China  
 2 (2023YFA1608100). We gratefully acknowledge the support of the National Natural Science Foun-  
 3 dation of China (NSFC, grant No. 12173037, 12233008, 11773063, 12288102, 12025303), the CAS  
 4 Project for Young Scientists in Basic Research (No. YSBR-092), the China Manned Space Project  
 5 with NO. CMS-CSST-2021-A02, CMS-CSST-2021-A04 and NO. CMS-CSST-2021-A06, the Funda-  
 6 mental Research Funds for the Central Universities (WK3440000006) and Cyrus Chun Ying Tang  
 7 Foundations. Yunkun Han also gratefully acknowledges the support from the National Key R&D  
 8 Program of China (Nos. 2021YFA1600401 and 2021YFA1600400), the “Light of West China” Pro-  
 9 gram of Chinese Academy of Sciences, the Yunnan Ten Thousand Talents Plan Young & Elite Talents  
 10 Project, the Natural Science Foundation of Yunnan Province (No. 202201BC070003), and the Inter-  
 11 national Centre of Supernovae, Yunnan Key Laboratory (No. 202302AN360001).

*Software:* astropy, BayeSED, emcee, GALIGHT, getdist

## APPENDIX

### A. IMAGE DECOMPOSITION RESULTS

**Table 2.** Decomposed host galaxy flux

Source	F435W	F606W	F775W	F814W	F850LP	F105W	F110W	F125W	F140W	F160W
	$\mu\text{Jy}$	$\mu\text{Jy}$	$\mu\text{Jy}$	$\mu\text{Jy}$	$\mu\text{Jy}$	$\mu\text{Jy}$	$\mu\text{Jy}$	$\mu\text{Jy}$	$\mu\text{Jy}$	$\mu\text{Jy}$
CID 108	..	< 3.32	..	$10.27 \pm 1.91$	..	..	..	$12.87 \pm 1.74$	..	$16.88 \pm 1.69$
CID 110	..	< 2.98	..	$11.35 \pm 0.37$	..	..	..	$21.22 \pm 0.44$	..	$26.71 \pm 0.94$
CID 128	..	..	..	$1.77 \pm 0.59$	..	$7.32 \pm 2.81$	..	$10.44 \pm 0.99$	..	$9.34 \pm 3.79$
CID 192	..	..	..	$4.48 \pm 0.11$	..	..	..	..	..	$12.70 \pm 0.21$
CID 1930	..	..	..	$0.48 \pm 0.46$	..	..	..	..	..	$20.82 \pm 1.26$
CID 216	..	..	..	$1.41 \pm 0.05$	..	..	..	..	$7.03 \pm 1.42$	..
CID 3570	..	..	..	..	..	..	..	$11.99 \pm 0.42$	..	..
CID 40	..	$3.53 \pm 1.58$	..	$4.39 \pm 1.85$	..	..	..	$8.87 \pm 1.75$	..	$17.74 \pm 1.63$
CID 597	..	..	..	$0.57 \pm 0.08$	..	..	..	..	..	..
CID 607	..	..	..	$0.94 \pm 0.09$	..	..	..	$3.20 \pm 0.27$	..	..
CID 644	..	..	..	$1.66 \pm 0.17$	..	..	..	..	..	$12.94 \pm 0.54$
CID 71	..	$7.57 \pm 0.12$	..	$23.92 \pm 0.29$	..	..	..	$48.64 \pm 1.07$	..	$63.59 \pm 0.50$
CID 72	..	$0.36 \pm 0.13$	..	$1.13 \pm 0.90$	..	..	..	$0.80 \pm 0.74$	$2.44 \pm 0.42$	$3.40 \pm 0.27$
CID 79	..	$2.13 \pm 0.16$	..	$2.20 \pm 0.03$	..	..	..	$9.99 \pm 0.21$	..	$13.24 \pm 0.15$
CID 87	..	< 0.20	..	$1.24 \pm 0.02$	..	..	..	$10.46 \pm 0.10$	..	$16.71 \pm 0.11$
ECDFS 379	$2.33 \pm 0.18$	$3.61 \pm 0.04$	$20.31 \pm 0.71$	$21.32 \pm 1.02$	$31.05 \pm 3.40$	..	..	$49.83 \pm 6.03$	$47.92 \pm 0.14$	$61.05 \pm 3.32$
ECDFS 391	$0.32 \pm 0.04$	$0.72 \pm 0.10$	$2.08 \pm 0.11$	$2.66 \pm 0.02$	$4.94 \pm 0.13$	..	..	$9.46 \pm 0.01$	$13.24 \pm 0.22$	$14.76 \pm 0.03$
LID 1273	..	..	..	$1.30 \pm 0.18$	..	..	..	..	$8.99 \pm 0.12$	..
LID 1820	..	..	..	..	..	..	..	..	$6.81 \pm 1.07$	..
LID 360	..	..	..	$0.79 \pm 0.47$	..	..	..	..	$9.10 \pm 1.31$	..
SXDS 0328	..	..	..	..	..	..	..	$11.28 \pm 1.11$	..	$14.90 \pm 2.32$
SXDS 0491	..	..	..	..	..	..	..	$10.11 \pm 0.50$	$13.18 \pm 0.59$	$16.81 \pm 1.36$
SXDS 0610	..	..	..	..	..	..	..	$12.52 \pm 0.12$	$14.27 \pm 0.81$	$18.31 \pm 0.68$
SXDS 0735	..	..	..	..	..	..	..	..	$7.02 \pm 0.26$	..

NOTE—(a) “..” means that data is not available for this band. (b) “< flux” means that this flux is an upper limit.

## REFERENCES

- Abuter, R., Allouche, F., Amorim, A., et al. 2024, *Nature*, 627, 281, doi: [10.1038/s41586-024-07053-4](https://doi.org/10.1038/s41586-024-07053-4)
- Ahumada, R., Allende Prieto, C., Almeida, A., et al. 2020, *ApJS*, 249, 3, doi: [10.3847/1538-4365/ab929e](https://doi.org/10.3847/1538-4365/ab929e)
- Anglés-Alcázar, D., Faucher-Giguère, C.-A., Quataert, E., et al. 2017, *MNRAS*, 472, L109, doi: [10.1093/mnrasl/slx161](https://doi.org/10.1093/mnrasl/slx161)
- Beifiori, A., Courteau, S., Corsini, E. M., & Zhu, Y. 2012, *MNRAS*, 419, 2497, doi: [10.1111/j.1365-2966.2011.19903.x](https://doi.org/10.1111/j.1365-2966.2011.19903.x)
- Bennert, V. N., Treu, T., Woo, J.-H., et al. 2010, *ApJ*, 708, 1507, doi: [10.1088/0004-637X/708/2/1507](https://doi.org/10.1088/0004-637X/708/2/1507)
- Birrer, S., & Amara, A. 2018, *Physics of the Dark Universe*, 22, 189, doi: [10.1016/j.dark.2018.11.002](https://doi.org/10.1016/j.dark.2018.11.002)
- Boquien, M., Burgarella, D., Roehly, Y., et al. 2018, *VizieR Online Data Catalog: Python Code Investigating GALaxy Emission (Boquien+, 2019), VizieR On-line Data Catalog: J/A+A/622/A103*. Originally published in: 2019A&A...622A.103B
- Bruzual, G., & Charlot, S. 2003, *MNRAS*, 344, 1000, doi: [10.1046/j.1365-8711.2003.06897.x](https://doi.org/10.1046/j.1365-8711.2003.06897.x)
- Calzetti, D., Armus, L., Bohlin, R. C., et al. 2000, *ApJ*, 533, 682, doi: [10.1086/308692](https://doi.org/10.1086/308692)
- Cen, R. 2015, *ApJ*, 805, L9, doi: [10.1088/2041-8205/805/1/L9](https://doi.org/10.1088/2041-8205/805/1/L9)
- Chabrier, G. 2003, *PASP*, 115, 763, doi: [10.1086/376392](https://doi.org/10.1086/376392)
- Chambers, K. C., Magnier, E. A., Metcalfe, N., et al. 2016, *arXiv e-prints*, arXiv:1612.05560, doi: [10.48550/arXiv.1612.05560](https://doi.org/10.48550/arXiv.1612.05560)



**Table 3.** Decomposed AGN point source flux

Source	F435W	F606W	F775W	F814W	F850LP	F105W	F110W	F125W	F140W	F160W
	$\mu\text{Jy}$	$\mu\text{Jy}$	$\mu\text{Jy}$	$\mu\text{Jy}$	$\mu\text{Jy}$	$\mu\text{Jy}$	$\mu\text{Jy}$	$\mu\text{Jy}$	$\mu\text{Jy}$	$\mu\text{Jy}$
CID 108	..	23.63 $\pm$ 2.36	..	16.58 $\pm$ 2.52	..	..	..	16.98 $\pm$ 1.46	..	24.67 $\pm$ 1.86
CID 110	..	6.36 $\pm$ 0.64	..	5.52 $\pm$ 0.08	..	..	..	9.40 $\pm$ 0.48	..	8.46 $\pm$ 0.18
CID 128	..	..	..	34.46 $\pm$ 0.64	..	39.38 $\pm$ 2.30	..	43.04 $\pm$ 0.70	..	60.68 $\pm$ 3.44
CID 192	..	..	..	17.08 $\pm$ 0.21	..	..	..	..	..	32.00 $\pm$ 0.30
CID 1930	..	..	..	29.96 $\pm$ 0.39	..	..	..	..	..	33.58 $\pm$ 0.93
CID 216	..	..	..	3.31 $\pm$ 0.06	..	..	..	..	4.18 $\pm$ 1.46	..
CID 3570	..	..	..	..	..	..	..	4.35 $\pm$ 0.49	..	..
CID 40	..	9.09 $\pm$ 1.59	..	10.11 $\pm$ 1.60	..	..	..	12.04 $\pm$ 1.44	..	11.35 $\pm$ 1.45
CID 597	..	..	..	11.07 $\pm$ 0.12	..	..	..	..	..	..
CID 607	..	..	..	27.94 $\pm$ 0.26	..	..	..	25.90 $\pm$ 0.28	..	..
CID 644	..	..	..	23.40 $\pm$ 0.40	..	..	..	..	..	11.72 $\pm$ 0.55
CID 71	..	9.84 $\pm$ 0.12	..	8.13 $\pm$ 0.21	..	..	..	11.66 $\pm$ 1.09	..	10.33 $\pm$ 0.42
CID 72	..	3.62 $\pm$ 0.15	..	5.08 $\pm$ 0.87	..	..	..	11.54 $\pm$ 0.77	10.21 $\pm$ 0.42	10.53 $\pm$ 0.29
CID 79	..	0.38 $\pm$ 0.13	..	1.08 $\pm$ 0.03	..	..	..	1.81 $\pm$ 0.25	..	1.45 $\pm$ 0.18
CID 87	..	0.24 $\pm$ 0.02	..	0.28 $\pm$ 0.03	..	..	..	1.91 $\pm$ 0.08	..	2.20 $\pm$ 0.05
ECDFS 379	58.82 $\pm$ 0.14	67.32 $\pm$ 0.41	63.31 $\pm$ 0.54	48.16 $\pm$ 0.79	63.74 $\pm$ 2.64	..	..	69.36 $\pm$ 4.59	63.81 $\pm$ 1.01	69.55 $\pm$ 2.63
ECDFS 391	12.75 $\pm$ 0.05	11.81 $\pm$ 0.00	11.01 $\pm$ 0.06	7.14 $\pm$ 0.04	9.06 $\pm$ 0.10	..	..	7.82 $\pm$ 0.01	9.70 $\pm$ 0.15	11.54 $\pm$ 0.02
LID 1273	..	..	..	26.58 $\pm$ 0.31	..	..	..	..	24.73 $\pm$ 0.19	..
LID 1820	..	..	..	..	..	..	..	..	11.51 $\pm$ 0.91	..
LID 360	..	..	..	50.23 $\pm$ 1.28	..	..	..	..	47.22 $\pm$ 1.26	..
SXDS 0328	..	..	..	..	..	..	..	14.76 $\pm$ 0.95	..	13.70 $\pm$ 1.98
SXDS 0491	..	..	..	..	..	..	..	8.69 $\pm$ 0.40	9.90 $\pm$ 0.64	11.81 $\pm$ 0.89
SXDS 0610	..	..	..	..	..	..	..	7.93 $\pm$ 0.16	6.98 $\pm$ 1.18	6.96 $\pm$ 0.58
SXDS 0735	..	..	..	..	..	..	..	..	44.00 $\pm$ 0.36	..

NOTE—“..” means that data is not available for this band.

Cross, N. J. G., Collins, R. S., Mann, R. G., et al. 2012, *A&A*, 548, A119, doi: [10.1051/0004-6361/201219505](https://doi.org/10.1051/0004-6361/201219505)

Cutri, R. M., Wright, E. L., Conrow, T., et al. 2021, *VizieR Online Data Catalog: AllWISE Data Release (Cutri+ 2013)*

DeGraf, C., Di Matteo, T., Treu, T., et al. 2015, *MNRAS*, 454, 913, doi: [10.1093/mnras/stv2002](https://doi.org/10.1093/mnras/stv2002)

Di Matteo, T., Colberg, J., Springel, V., Hernquist, L., & Sijacki, D. 2008, *ApJ*, 676, 33, doi: [10.1086/524921](https://doi.org/10.1086/524921)

Ding, X., Birrer, S., Treu, T., & Silverman, J. D. 2021, *arXiv e-prints*, arXiv:2111.08721, doi: [10.48550/arXiv.2111.08721](https://doi.org/10.48550/arXiv.2111.08721)

Ding, X., Silverman, J., Treu, T., et al. 2020, *ApJ*, 888, 37, doi: [10.3847/1538-4357/ab5b90](https://doi.org/10.3847/1538-4357/ab5b90)

Ding, X., Onoue, M., Silverman, J. D., et al. 2023, *Nature*, 621, 51, doi: [10.1038/s41586-023-06345-5](https://doi.org/10.1038/s41586-023-06345-5)

Ferrarese, L., & Merritt, D. 2000, *ApJ*, 539, L9, doi: [10.1086/312838](https://doi.org/10.1086/312838)

Gebhardt, K., Lauer, T. R., Kormendy, J., et al. 2001, *AJ*, 122, 2469, doi: [10.1086/323481](https://doi.org/10.1086/323481)

Hambly, N. C., Collins, R. S., Cross, N. J. G., et al. 2008, *MNRAS*, 384, 637, doi: [10.1111/j.1365-2966.2007.12700.x](https://doi.org/10.1111/j.1365-2966.2007.12700.x)

Han, Y., Fan, L., Zheng, X. Z., Bai, J.-M., & Han, Z. 2023, *ApJS*, 269, 39, doi: [10.3847/1538-4365/acfc3a](https://doi.org/10.3847/1538-4365/acfc3a)

Han, Y., & Han, Z. 2014, *ApJS*, 215, 2, doi: [10.1088/0067-0049/215/1/2](https://doi.org/10.1088/0067-0049/215/1/2)

—. 2018, *ApJS*, 240, 3, doi: [10.3847/1538-4365/aaeffa](https://doi.org/10.3847/1538-4365/aaeffa)

Häring, N., & Rix, H.-W. 2004, *ApJ*, 604, L89, doi: [10.1086/383567](https://doi.org/10.1086/383567)

Harrison, C. M. 2017, *Nature Astronomy*, 1, 0165, doi: [10.1038/s41550-017-0165](https://doi.org/10.1038/s41550-017-0165)

Hirschmann, M., Khochfar, S., Burkert, A., et al. 2010, *MNRAS*, 407, 1016, doi: [10.1111/j.1365-2966.2010.17006.x](https://doi.org/10.1111/j.1365-2966.2010.17006.x)

Hopkins, P. F., Cox, T. J., Kereš, D., & Hernquist, L. 2008, *ApJS*, 175, 390, doi: [10.1086/524363](https://doi.org/10.1086/524363)

Jahnke, K., & Macciò, A. V. 2011, *ApJ*, 734, 92, doi: [10.1088/0004-637X/734/2/92](https://doi.org/10.1088/0004-637X/734/2/92)

Jahnke, K., Bongiorno, A., Brusa, M., et al. 2009, *ApJ*, 706, L215, doi: [10.1088/0004-637X/706/2/L215](https://doi.org/10.1088/0004-637X/706/2/L215)

- Kim, M., Ho, L. C., Peng, C. Y., Barth, A. J., & Im, M. 2017, *ApJS*, 232, 21, doi: [10.3847/1538-4365/aa8a75](https://doi.org/10.3847/1538-4365/aa8a75)
- Komatsu, E., Smith, K. M., Dunkley, J., et al. 2011, *ApJS*, 192, 18, doi: [10.1088/0067-0049/192/2/18](https://doi.org/10.1088/0067-0049/192/2/18)
- Kormendy, J., & Ho, L. C. 2013, *ARA&A*, 51, 511, doi: [10.1146/annurev-astro-082708-101811](https://doi.org/10.1146/annurev-astro-082708-101811)
- Lauer, T. R., Tremaine, S., Richstone, D., & Faber, S. M. 2007, *ApJ*, 670, 249, doi: [10.1086/522083](https://doi.org/10.1086/522083)
- Lawrence, A., Warren, S. J., Almaini, O., et al. 2007, *MNRAS*, 379, 1599, doi: [10.1111/j.1365-2966.2007.12040.x](https://doi.org/10.1111/j.1365-2966.2007.12040.x)
- Li, J., Silverman, J. D., Ding, X., et al. 2021a, *ApJ*, 922, 142, doi: [10.3847/1538-4357/ac2301](https://doi.org/10.3847/1538-4357/ac2301)
- . 2021b, *ApJ*, 918, 22, doi: [10.3847/1538-4357/ac06a8](https://doi.org/10.3847/1538-4357/ac06a8)
- Li, J., Silverman, J. D., Shen, Y., et al. 2024, arXiv e-prints, arXiv:2403.00074, doi: [10.48550/arXiv.2403.00074](https://doi.org/10.48550/arXiv.2403.00074)
- Li, J. I. H., Shen, Y., Ho, L. C., et al. 2023, *ApJ*, 954, 173, doi: [10.3847/1538-4357/acddd4](https://doi.org/10.3847/1538-4357/acddd4)
- Magorrian, J., Tremaine, S., Richstone, D., et al. 1998, *AJ*, 115, 2285, doi: [10.1086/300353](https://doi.org/10.1086/300353)
- Marconi, A., & Hunt, L. K. 2003, *ApJ*, 589, L21, doi: [10.1086/375804](https://doi.org/10.1086/375804)
- Martin, D. C., Fanson, J., Schiminovich, D., et al. 2005, *ApJ*, 619, L1, doi: [10.1086/426387](https://doi.org/10.1086/426387)
- Matsuoka, Y., Strauss, M. A., Shen, Y., et al. 2015, *ApJ*, 811, 91, doi: [10.1088/0004-637X/811/2/91](https://doi.org/10.1088/0004-637X/811/2/91)
- Menci, N., Fiore, F., Bongiorno, A., & Lamastra, A. 2016, *A&A*, 594, A99, doi: [10.1051/0004-6361/201628415](https://doi.org/10.1051/0004-6361/201628415)
- Momcheva, I. G., Brammer, G. B., van Dokkum, P. G., et al. 2016, *ApJS*, 225, 27, doi: [10.3847/0067-0049/225/2/27](https://doi.org/10.3847/0067-0049/225/2/27)
- Netzer, H. 2015, *ARA&A*, 53, 365, doi: [10.1146/annurev-astro-082214-122302](https://doi.org/10.1146/annurev-astro-082214-122302)
- Noll, S., Burgarella, D., Giovannoli, E., et al. 2009, doi: [10.1051/0004-6361/200912497](https://doi.org/10.1051/0004-6361/200912497)
- Park, D., Woo, J.-H., Bennert, V. N., et al. 2015, *ApJ*, 799, 164, doi: [10.1088/0004-637X/799/2/164](https://doi.org/10.1088/0004-637X/799/2/164)
- Peng, C. Y. 2007, *ApJ*, 671, 1098, doi: [10.1086/522774](https://doi.org/10.1086/522774)
- Peng, C. Y., Ho, L. C., Impey, C. D., & Rix, H.-W. 2002, *AJ*, 124, 266, doi: [10.1086/340952](https://doi.org/10.1086/340952)
- Schramm, M., & Silverman, J. D. 2013, *ApJ*, 767, 13, doi: [10.1088/0004-637X/767/1/13](https://doi.org/10.1088/0004-637X/767/1/13)
- Schulze, A., & Wisotzki, L. 2011, *A&A*, 535, A87, doi: [10.1051/0004-6361/201117564](https://doi.org/10.1051/0004-6361/201117564)
- Schulze, A., Bongiorno, A., Gavignaud, I., et al. 2015, *MNRAS*, 447, 2085, doi: [10.1093/mnras/stu2549](https://doi.org/10.1093/mnras/stu2549)
- Schulze, A., Silverman, J. D., Kashino, D., et al. 2018, *ApJS*, 239, 22, doi: [10.3847/1538-4365/aae82f](https://doi.org/10.3847/1538-4365/aae82f)
- Setoguchi, K., Ueda, Y., Toba, Y., et al. 2024, *ApJ*, 961, 246, doi: [10.3847/1538-4357/ad1186](https://doi.org/10.3847/1538-4357/ad1186)
- Springel, V., Di Matteo, T., & Hernquist, L. 2005, *MNRAS*, 361, 776, doi: [10.1111/j.1365-2966.2005.09238.x](https://doi.org/10.1111/j.1365-2966.2005.09238.x)
- Suh, H., Civano, F., Trakhtenbrot, B., et al. 2020, *ApJ*, 889, 32, doi: [10.3847/1538-4357/ab5f5f](https://doi.org/10.3847/1538-4357/ab5f5f)
- Suh, H., Civano, F., Hasinger, G., et al. 2019, *ApJ*, 872, 168, doi: [10.3847/1538-4357/ab01fb](https://doi.org/10.3847/1538-4357/ab01fb)
- Sun, M., Trump, J. R., Brandt, W. N., et al. 2015, *ApJ*, 802, 14, doi: [10.1088/0004-637X/802/1/14](https://doi.org/10.1088/0004-637X/802/1/14)
- Sun, W., Fan, L., Han, Y., et al. 2024, *ApJ*, 964, 95, doi: [10.3847/1538-4357/ad22e3](https://doi.org/10.3847/1538-4357/ad22e3)
- Tanaka, T. S., Silverman, J. D., Ding, X., et al. 2024, arXiv e-prints, arXiv:2401.13742, doi: [10.48550/arXiv.2401.13742](https://doi.org/10.48550/arXiv.2401.13742)
- Trakhtenbrot, B., & Netzer, H. 2012, *MNRAS*, 427, 3081, doi: [10.1111/j.1365-2966.2012.22056.x](https://doi.org/10.1111/j.1365-2966.2012.22056.x)
- Treu, T., Malkan, M. A., & Blandford, R. D. 2004, *ApJ*, 615, L97, doi: [10.1086/426437](https://doi.org/10.1086/426437)
- Treu, T., Woo, J.-H., Malkan, M. A., & Blandford, R. D. 2007, *ApJ*, 667, 117, doi: [10.1086/520633](https://doi.org/10.1086/520633)
- Vestergaard, M., & Peterson, B. M. 2006, *ApJ*, 641, 689, doi: [10.1086/500572](https://doi.org/10.1086/500572)
- Whitmore, B. C., Allam, S. S., Budavári, T., et al. 2016, *AJ*, 151, 134, doi: [10.3847/0004-6256/151/6/134](https://doi.org/10.3847/0004-6256/151/6/134)
- Yang, G., Brandt, W. N., Vito, F., et al. 2018, *MNRAS*, 475, 1887, doi: [10.1093/mnras/stx2805](https://doi.org/10.1093/mnras/stx2805)
- Zhuang, M.-Y., & Ho, L. C. 2023, *Nature Astronomy*, 7, 1376, doi: [10.1038/s41550-023-02051-4](https://doi.org/10.1038/s41550-023-02051-4)
- Zhuang, M.-Y., Li, J., & Shen, Y. 2024, *ApJ*, 962, 93, doi: [10.3847/1538-4357/ad1517](https://doi.org/10.3847/1538-4357/ad1517)
- Zou, F., Yang, G., Brandt, W. N., & Xue, Y. 2019, *ApJ*, 878, 11, doi: [10.3847/1538-4357/ab1eb1](https://doi.org/10.3847/1538-4357/ab1eb1)